Available online at www.sciencedirect.com
ScienceDirect
International Journal of Thermal Sciences 47 (2008) 569–583
International Journal of Thermal Sciences
www.elsevier.com/locate/ijts

Natural convection in a porous enclosure with a partial heating and salting element

Fu-Yun Zhao, Di Liu, Guang-Fa Tang *

College of Civil Engineering, Hunan University, Changsha, Hunan 410082, PR China

Received 6 December 2006; received in revised form 20 April 2007; accepted 24 April 2007

Available online 20 June 2007

Abstract

This paper reports a numerical study of double-diffusive convective flow of a binary mixture in a porous enclosure subject to localized heating and salting from one side. The physical model for the momentum conservation equation makes use of the Darcy–Brinkman equation, which allows the no-slip boundary condition on a solid wall to be satisfied. The set of coupled equations is solved using the SIMPLE algorithm. An extensive series of numerical simulations is conducted in the range of $-15 \leqslant N \leqslant +14$, $10^{-3} \leqslant Le \leqslant 10^{2}$, $10^{-8} \leqslant Da \leqslant 10^{2}$ and $0.125 \leqslant L \leqslant 0.875$, where N, Le, Da and L are the buoyancy ratio, Lewis number, Darcy number and the segment location. Results for a pure viscous fluid and a Darcy (densely packed) porous medium emerge from the present model as limiting cases. Streamlines, heatlines, masslines, isotherms and iso-concentrations are produced for several segment locations to illustrate the flow structure transition from solutal-dominated opposing to thermal dominated and solutal-dominated aiding flows, respectively. The segment location combining with Lewis number is found to influence the buoyancy ratio at which flow transition and flow reversal occurs. The computed overall Nusselt and Sherwood numbers provide guidance for locating the heating and salting segment.

Keywords: Natural convection; Heatlines and masslines; Discrete source; Porous medium; Enclosure flows

1. Introduction

The study of flow caused by the combined influence of thermal and mass buoyancy forces through porous medium has been motivated by its importance in many natural and industrial problems. Some of these are the migration of moisture through air contained in fibrous insulation, chemical transport in packed-bed reactors, melting and solidification of binary alloys, grain storage, food processing and storage, contaminant transport in ground water, to name just a few. Relative to a large volume of published studies on this phenomenon in pure fluids, the thermosolutal convection in porous media has received only limited attention. A comprehensive review of the literature concerning double-diffusive natural convection in a fluid-saturated porous medium may be found in the book by Ingham and Pop [1]. The literature review indicates that double diffusive natural convection in vertical enclosures completely filled with fluid-saturated porous media has been the subject of a vast number of studies. In these studies, the following boundary conditions (imposed along the vertical boundaries) have been studied,

- Subject to constant temperature and concentration, such as Refs. [2–11].
- Subject to uniform heat and mass fluxes, such as Refs. [12–18].
- Subject to uniform heat/mass fluxes and constant temperature/concentration simultaneously (mixing Dirichlet and Neumann boundary conditions), such as Refs. [12,19].

Besides, the linear distributions of temperature and concentration along the vertical side have been considered by Kumar and his co-authors [20,21]. In fact, many engineering systems may be characterized by double-diffusive behavior induced by concentrated heat and solute sources on one side, such as building construction elements with passive solar heating and conta-

* Corresponding author. Tel.: +86 731 8822760; fax: +86 731 8822667.
E-mail addresses: zfycfdnet@163.com (F.-Y. Zhao), liudi66@163.com (D. Liu), gftangcfd@163.com (G.-F. Tang).

1290-0729/$ – see front matter
doi:10.1016/j.ijthermalsci.2007.04.006

Nomenclature

AR	aspect ratio (W/H)	
B	dimensionless length of segment (b/H)	
D	mass diffusivity	m^2/s
Da	Darcy number (K/H^2)	
g	gravitational acceleration	m/s^2
H	height of the enclosure	m
k	thermal conductivity of the porous medium	$W/(m\,K)$
K	permeability of the porous medium	m^2
L	dimensionless position of segment (l/H)	
Le	Lewis number (α/D)	
N	buoyancy ratio (Eq. (13))	
Nu	overall Nusselt number (Eq. (15))	
P	fluid pressure	N/m^2
Pr	Prandtl number (ν/α)	
Ra	thermal Rayleigh number (Eq. (13))	
s	dimensional mass fraction	
Sh	overall Sherwood number (Eq. (15))	
T	temperature	K
u	velocity components in x direction	m/s
v	velocity components in y direction	m/s
W	width of the enclosure	m
x, y	Cartesian coordinates	m

Greek symbols

α	thermal diffusivity	m^2/s
β_t	thermal expansion coefficient	1/K
β_s	expansion coefficient with mass fraction	
Δ	difference value	
ν	kinematic viscosity	m^2/s
ρ	fluid density	kg/m^3
τ	dimensionless time (Eq. (7a))	
Φ	generic variable (U, V, T or S)	
Ψ	dimensionless streamfunction	
ξ	dimensionless heatfunction	
η	dimensionless massfunction	

Subscripts

max, min	maximum, minimum
o	reference value or location
s	solutal
t	thermal

Superscripts

$*$	dimensional variable

minant infiltration, hazardous thermo-chemical spreading, solar pond and liquid fuel storage tank. Though it has been received extensive attentions in pure natural convection heat transfer [22, 23] and for enclosures subject to cross gradients of temperature and concentration [24,25], to the best of the authors' knowledge, there are few published results about the double diffusive natural convection in a vertical porous enclosure partially heated and salted from one side [26].

Additionally, in previous works, the porous medium was modeled using the Darcy flow model [2,4,5,7,10,12–24,26,27]. Darcy's Law is a good approximation for low-porosity media. However, for large values of Darcy number, Darcy's model may over-predict the convective flows because it cannot account for the inertia effects and the no-slip boundary conditions on rigid boundaries. Recently, the Darcy–Brinkman formulation has been used to study the influence of the Darcy number on the double-diffusive natural convection within a rectangular porous cavity [3,6–9,11]. It was found that the behavior of the thermosolutal flow in porous media was different from the behavior assessed for fluid. The porous medium considered here is thus modeled according to the Darcy–Brinkman formulation.

In order to delineate the characteristics of fluid flow and the associated heat and mass transfer in the porous enclosure, preceding authors presented diverse solution methods, including scale analysis [2,3,7,13], closed-form analytical solutions [12–14,16–18] and full numerical solutions [2–24,26]. Due to constraints of scale analysis and parallel flow approximation, discrete numerical experiments would be conducted to study the double diffusive natural convection occurring inside this porous cavity. Simultaneously, visualization of the heat and solute transports, using streamlines, heatlines and masslines [10,25–30], would be conducted in the present work.

The specific problem considered here is the study of double diffusive convection within a square enclosure subject to the heating and salting segment on one side. In following sections, the physical model and mathematical formulation for the problem is first given. Subsequently, a numerical simulation of the full governing equations is carried out to study the transport structures and heat/mass transfer rates. Finally, the results from the numerical computations are discussed in detail.

2. Physical model and problem statements

The physical domain under investigation is a two-dimensional fluid-saturated Darcy–Brinkman porous enclosure (see Fig. 1). The rectangular enclosure is of width W and height H, and the Cartesian coordinates (x, y), with the corresponding velocity components (u, v), are indicated herein. It is assumed that the third dimension of the enclosure is large enough so that the fluid, heat and mass transports are two-dimensional. The top and bottom boundaries of the enclosure are thermally insulated and impermeable. At the right wall a heating and salting segment of length b is subjected to higher and constant temperature and concentration, t_1 and s_1, while the rest of it is insulated and impermeable. The distance between the center of the heating and salting segment and the bottom wall is l, such that when $l = H/2$ the segment is centrally located at the right sidewall. The opposing vertical wall is maintained lower temperature and concentration constants, t_0 and s_0. Gravity acts in the negative y-direction.

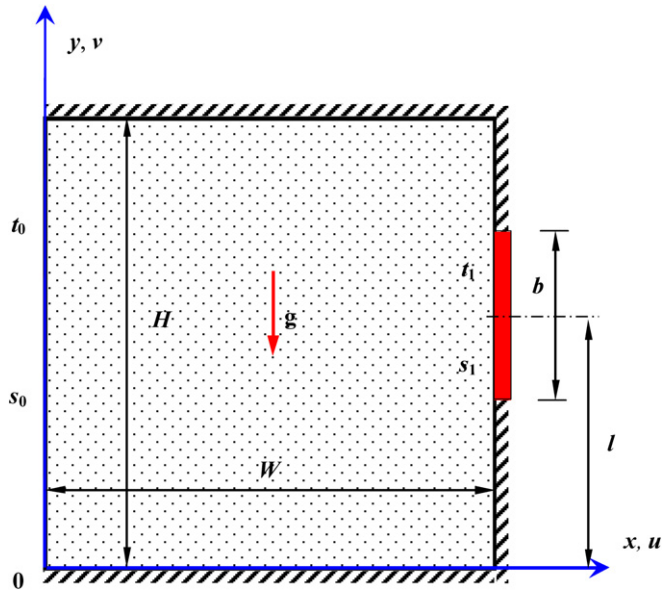

Fig. 1. Flow configuration and coordinate system.

The porous matrix is assumed to be uniform and in local thermal and compositional equilibrium with the saturating fluid. Thermophysical properties are supposed constant. The flow is assumed to be laminar and incompressible. Viscous dissipation and porous medium inertia are not considered, and the Soret and Dufour effects are neglected. Density of the saturated fluid mixture is assumed to be uniform over all the enclosure, exception made to the buoyancy term, in which it is taken as a function of both the temperature t and concentration s through the Boussinesq approximation,

$$\rho = \rho_0\left[1 - \beta_t(t - t_0) - \beta_s(s - s_0)\right] \tag{1}$$

Where ρ_0 is the fluid density at temperature t_0 and concentration s_0, and β_t and β_s are the thermal and concentration expansion coefficients, respectively. Subscript 0 refers to the condition over the left vertical wall of the enclosure.

By employing the aforementioned assumptions into the macroscopic conservation equations of mass, momentum, energy and species, a set of dimensionless governing equations is obtained as,

$$\frac{\partial U}{\partial X} + \frac{\partial V}{\partial Y} = 0 \tag{2}$$

$$\frac{\partial U}{\partial \tau} + \frac{\partial UU}{\partial X} + \frac{\partial VU}{\partial Y} = -\frac{\partial P}{\partial X} + \sqrt{\frac{Pr}{Ra}}\left(\frac{\partial^2 U}{\partial X^2} + \frac{\partial^2 U}{\partial Y^2}\right) - \sqrt{\frac{Pr}{Ra}}\frac{U}{Da} \tag{3}$$

$$\frac{\partial V}{\partial \tau} + \frac{\partial UV}{\partial X} + \frac{\partial VV}{\partial Y} = -\frac{\partial P}{\partial Y} + \sqrt{\frac{Pr}{Ra}}\left(\frac{\partial^2 V}{\partial X^2} + \frac{\partial^2 V}{\partial Y^2}\right) - \sqrt{\frac{Pr}{Ra}}\frac{V}{Da} + (T + NS) \tag{4}$$

$$\frac{\partial T}{\partial \tau} + \frac{\partial UT}{\partial X} + \frac{\partial VT}{\partial Y} = \frac{1}{\sqrt{Ra\,Pr}}\left(\frac{\partial^2 T}{\partial X^2} + \frac{\partial^2 T}{\partial Y^2}\right) \tag{5}$$

$$\frac{\partial S}{\partial \tau} + \frac{\partial US}{\partial X} + \frac{\partial VS}{\partial Y} = \frac{1}{Le\sqrt{Ra\,Pr}}\left(\frac{\partial^2 S}{\partial X^2} + \frac{\partial^2 S}{\partial Y^2}\right) \tag{6}$$

The following dimensionless variables are used [31,32],

$$(X, Y) = (x, y)/H, \qquad (U, V) = (u, v)/V_r$$
$$\tau = \tau^*/(H/V_r) \tag{7a}$$
$$P = (p + \rho_0 g y)/\left(\rho V_r^2\right), \qquad T = (t - t_0)/\Delta t$$
$$S = (s - s_0)/\Delta s \tag{7b}$$

$$V_r = (g\beta_t \Delta t H)^{1/2}, \qquad \Delta t = t_1 - t_0, \qquad \Delta s = s_1 - s_0 \tag{8}$$

Where H, V_r, H/V_r, Δt, and Δs are the scales for length, velocity, time, temperature and concentration respectively. The boundary conditions sketched in Fig. 1 are,

$$X = 0, \qquad U = V = 0, \qquad T = 0, \qquad S = 0 \tag{9}$$

$$Y = 0 \text{ and } 1, \qquad U = V = 0, \qquad \frac{\partial T}{\partial Y} = 0, \qquad \frac{\partial S}{\partial Y} = 0 \tag{10}$$

$$X = AR \text{ and } L - B/2 \leqslant Y \leqslant L + B/2, \qquad U = V = 0$$
$$T = 1, \qquad S = 1 \tag{11}$$

$$X = AR \text{ and } 0 \leqslant Y \leqslant L - B/2, \qquad L + B/2 \leqslant Y \leqslant 1$$
$$U = V = 0, \qquad \frac{\partial T}{\partial X} = 0, \qquad \frac{\partial S}{\partial X} = 0 \tag{12}$$

Eqs. (2)–(6) indicate that the present problem is governed by the following dimensionless parameters, namely, Prandtl number Pr, Darcy number Da, the thermal Rayleigh number Ra, the solutal to thermal buoyancy ratio N and Lewis number Le defined as,

$$Pr = \nu/\alpha, \qquad Da = K/H^2, \qquad Ra = g\beta_t \Delta t H^3/\nu\alpha$$
$$N = \beta_s \Delta s/\beta_t \Delta t, \qquad Le = \alpha/D \tag{13}$$

Where ν is the kinematics viscosity of the fluid, α and D respectively are the thermal and molecular diffusivities of the combined fluid plus solid porous matrix medium, K is the permeability of the porous medium, and g is the acceleration due to gravity. Since the particle Reynolds number is considered being less than unity in this work, the Forchheimer inertia term has been dropped from the momentum equations (3) and (4) compared with the Darcy and Brinkman terms. The porosity of the porous layer, the ratios between effective viscosity and fluid viscosity, and the ratios of the thermophysical properties of the porous medium and of the fluid, have been implicitly set to unity [3].

The thermal Rayleigh number Ra is usual when analyzing the single natural convection heat transfer in porous enclosure [23]. The porous thermal Rayleigh number R_t, defined as $R_t = Ra\,Da$, will also be used in the analysis. In addition, the buoyancy ratio N and Lewis number Le arise when analyzing the double-diffusive natural convection problems. The buoyancy ratio N denotes the relative strengths of the thermal and solutal buoyancy forces, and it can be either positive or negative, its sign depending on the ratio of β_s and β_t. The volumetric expansion coefficient due to temperature change β_t is normally positive, the water in the range 0–4.1°C being the most frequent

exception; But the volumetric expansion coefficient for concentration β_s can be either positive ($N > 0$) or negative ($N < 0$), such as moist air [10]. For the boundary conditions prescribed by Eqs. (9)–(12), the thermal and solute buoyancy effects are augmented when N is positive, and they are opposed otherwise. Further, N is zero for non-species effect and infinite for solute-dominated effect. Combined global heat and solute flows and negative values of parameter N can lead to multiple solutions or oscillatory solutions [4,8,14–16,19,24], such situations are intentionally avoided in the present work.

From the above boundary conditions, Eqs. (9)–(12), and geometry of the enclosure, it appears that the present problem is simultaneously governed by additional three dimensionless geometry parameters, cavity aspect ratio AR, length of the heating and salting segment B and the distance L, which are defined respectively as,

$$AR = W/H, \qquad B = b/H, \qquad L = l/H \tag{14}$$

The case $L = 1/2$, $B < 1$ corresponds to a porous enclosure with the heating and salting segment located centrally at the vertical side.

3. Convective transport evaluation and visualization

The overall heat and mass transfer rates across the system are important in engineering applications. It is appropriate at this stage to define the Nusselt and Sherwood numbers on the surface of heat and mass sinks can be written respectively as,

$$Nu = \int_0^1 -\frac{\partial T}{\partial X}\bigg|_{X=0} \mathrm{d}Y, \qquad Sh = \int_0^1 -\frac{\partial S}{\partial X}\bigg|_{X=0} \mathrm{d}Y \tag{15}$$

Streamfunction and streamlines are routinely the best way to visualize the convective fluid flow. The dimensionless streamfunction Ψ is defined such that,

$$\frac{\partial \Psi}{\partial Y} = U, \qquad -\frac{\partial \Psi}{\partial X} = V \tag{16}$$

The heat and mass transport processes are analyzed through the heatlines and masslines, respectively [10,25–30]. The heatfunction and massfunction can be made dimensionless respectively as [27,29],

$$\xi = \xi^*/[k\Delta t], \qquad \eta = \eta^*/[\rho D \Delta s] \tag{17}$$

The dimensionless first order derivatives of heatfunction and massfunction equations can be obtained as follows,

$$\begin{aligned} \frac{\partial \xi}{\partial Y} &= \sqrt{Ra\,Pr}\,UT - \frac{\partial T}{\partial X} \\ -\frac{\partial \xi}{\partial X} &= \sqrt{Ra\,Pr}\,VT - \frac{\partial T}{\partial Y} \end{aligned} \tag{18}$$

$$\begin{aligned} \frac{\partial \eta}{\partial Y} &= Le\sqrt{Ra\,Pr}\,US - \frac{\partial S}{\partial X} \\ -\frac{\partial \eta}{\partial X} &= Le\sqrt{Ra\,Pr}\,VS - \frac{\partial S}{\partial Y} \end{aligned} \tag{19}$$

The ξ and η fields are defined through its first order derivatives, being thus important only differences in its values but not its level, which is similar to the flow field defined by Eq. (16). Thus, we have the freedom to state that,

$$\Psi(0,0) = \xi(0,0) = \eta(0,0) = 0 \tag{20}$$

The heat and mass functions are evaluated for visualization purposes, once known the flow, temperature and concentration fields, they can be obtained using the solution method for conduction-type problems [27–30]. Due to the aforementioned dimensionless form of the heatfunction and massfunction, the numerical values of such functions along the top horizontal wall can match global Nusselt and Sherwood numbers respectively, that is to say, the overall heat and mass transfer rates across the system would be provided directly by the heatline and massline on the top wall [28,29]. Strictly, heatlines and masslines can be used only for two-dimensional steady problems without source terms. However, considering that, at a given instant, the differential energy conservation equation without the unsteady term can be taken to describe the heat transfer problem, the heatline concept can be applied without problems to such an equation [30]. Similar considerations are made for the use of the masslines for unsteady problems.

4. Numerical technique and code validation

A FVM (Finite Volume method) was used to obtain numerical solutions of the complete governing equations (2)–(6) on a staggered grid system [33]. In the course of discretization, the third-order deferred correction QUICK scheme [34] and a second-order central difference scheme are respectively implemented for the convection and diffusion terms. The SIMPLE algorithm was chosen to numerically solve the governing differential equations in their primitive form. The pressure correction equation is derived from the continuity equation to enforce the local mass balance [33,35]. To obtain better convergence properties, the unsteady terms in these equations are implicitly treated and hence approximated by backward differencing. For each time step, the discretized equations are solved using a line-by-line procedure, combining the tri-diagonal matrix algorithm (TDMA) and the successive over-relaxation (SOR) iteration. The permanent solution has been obtained by this false transient procedure. The iterative procedure is repeated until the following condition is satisfied,

$$\frac{\sum_i \sum_j |\Phi_{i,j}^{\mathrm{new}} - \Phi_{i,j}^{\mathrm{old}}|}{\sum_i \sum_j |\Phi_{i,j}^{\mathrm{new}}|} \leqslant 10^{-4} \tag{21}$$

Where Φ stands for U, V, T and S. The subscript i and j indices denote grid locations in the (X, Y) plane. A further decrease of the convergence criteria 10^{-4} does not cause any significant change in the final results.

Simultaneously, reliable numerical results are obtained by performing an energy balance at each time step over the physical domain [22,29]. For a steady flow condition the heat transfer through each plane $X =$ constant was evaluated at each location $0 \leqslant X \leqslant 1$ and compared with that of the input ($X = 1$) and the output ($X = 0$). A similar test was conducted to verify the overall mass balance. As the horizontal walls are impermeable and adiabatic, the thermal and solute conservations of the

two-dimensional isolated and impermeable system illustrated in Fig. 1 can be written in mathematical forms respectively as follows [31],

$$\int_{(L-B/2)}^{(L+B/2)} -\left.\frac{\partial T}{\partial X}\right|_{X=1} \mathrm{d}Y - Nu = 0$$

$$\int_{(L-B/2)}^{(L+B/2)} -\left.\frac{\partial S}{\partial X}\right|_{X=1} \mathrm{d}Y - Sh = 0 \tag{22}$$

For most of the results reported here, the energy and mass balances, Eq. (22), were satisfied to within 0.1%.

In order to resolve the boundary layers along the surfaces of heat and solute sources, non-uniform grids in X and Y direction were used for all computations and the grid was clustered toward the sidewalls, especially for the case of large Le. A systematic grid independence study was conducted, and then the final grid resolution of 81×81 was selected at the balance between the calculation accuracy and the speed for $AR = 1$.

The current numerical technique has been very successfully used in a series of recent papers, including single-component natural convection [31,32], conjugate heat transfer [28,29,31, 32], double diffusive natural convection [29] and mixed convection [25] in gaseous enclosures. To further validate the present numerical code, the double diffusive natural convection in square uniform porous enclosures has been numerically analyzed. One of the initial numerical studies on double diffusive natural convection in Darcy porous enclosure was performed by Goyeau et al. [3], Bennacer et al. [7] and Bourich et al. [24]. For this comparison, solutions presented in Table 1 are obtained for $R_t = 10^2 - 2.0 \times 10^3$, $Le = 10, 10^2$ in a square cavity where the two vertical walls are maintained at uniform and different temperatures and concentrations, while the horizontal walls are impermeable and adiabatic. In this configuration, the solutal buoyancy force is not presented ($N = 0$), but mass transfer is induced by the thermally driven flow, i.e., heat-transfer-driven flows. This means that the temperature field is coupled to the flow field and not coupled to the concentration field. More results concerning the Darcy model in the $N = 0$ situation on a range of Le and R_t values are displayed in Table 1. As expected, the Nusselt number does not depend on the Lewis number for a given R_t, since the flow is totally driven by the thermal buoyancy force. On the other hand, the Sherwood number is clearly seen to increase with increasing Le or R_t numbers. In general, the results are in good agreement with those of Goyeau et al. [3], Bennacer et al. [7] and Bourich et al. [24], thereby providing validation to our simulations.

Uniform heat transfer flux and constant concentration difference, i.e., mixed boundary conditions, are applied to the vertical walls. A comparison of the results for heat-transfer-driven flow may be found in Table 2, for this case the Nusselt number will also be independent of Lewis number. The agreement between the present study and Trevisan and Bejan [12]'s results for mixed boundary conditions is fairly good.

Kumar et al. [20] have employed Finite Element method to study the combined heat and mass transfer by natural convection in a Darcy porous enclosure. Flow fields computed by the present code are identical to the steady ones from Kumar et al. [20], particularly for isotherms and streamlines as $R_t = 100$, $Le = 1$, $N = -4, -1.5, -0.5, 0.5, 1.5, 4$, and for isoconcentrations as $R_t = 100$, $N = 0$, $Le = 0.1, 0.4, 1.0, 10, 25, 100$. Chamkha and his coauthors [8,9] have employed Finite Difference method to study the laminar double diffusive convective flow of a binary gas mixture in a rectangular enclosure filled with a uniform Darcy–Brinkman porous medium. For no inner heat sources, and with $Le = 1$, $Pr = 0.7$, $Ra = 10^5$, $N = 1.0$, $1/Da = 0, 10^2, 10^3, 10^4$, the average Nusselt (Sherwood) numbers obtained by Chamkha [9] are 6.08899, 5.59823, 3.59821 and 1.26309. The corresponding average Nusselt (Sherwood) numbers obtained with the present code are respectively 6.0932, 5.6093, 3.6100, and 1.2758, yielding less than 0.5% difference.

Table 1
Total Nusselt and Sherwood numbers compared with those of Goyeau et al. [3], Bennacer et al. [7] and Bourich et al. [24] for the case of isotropic porous media on heat-transfer-driven flows (Darcy model: $N = 0$, $AR = 1$, $B = 1$)

	R_t					Le	
	100	200	400	1000	2000	10	
Goyeau et al. [3]	3.11	4.96	7.77	13.47	19.90		*Nu*
	13.25	19.86	28.41	48.32	69.29		*Sh*
Bennacer et al. [7]	3.11	4.96	7.77	13.48	19.89		*Nu*
	13.24	19.83	29.36	48.20	69.08		*Sh*
Bourich et al. [24]	3.11	4.96	–	13.76	–		*Nu*
	13.27	20.02	–	47.40	–		*Sh*
Present work	3.10	4.93	7.71	13.45	20.01		*Nu*
	13.23	19.93	29.76	49.76	72.64		*Sh*
	100	200	400	1000	2000	100	
Goyeau et al. [3]	3.11	4.96	–	13.47	19.90		*Nu*
	41.53	61.09	–	140.65	196.62		*Sh*
Bennacer et al. [7]	–	–	–	13.48	19.89		*Nu*
	–	–	–	139.93	195.37		*Sh*
Present work	3.09	4.92	7.71	13.45	20.01		*Nu*
	42.84	63.33	93.78	145.96	210.39		*Sh*

Table 2
Numerical results for heat-transfer-driven natural convection in a porous layer with mixed boundary conditions, constant heat flux and constant concentration, along the vertical sides (Darcy model: $N = 0$, $AR = 1$, $B = 1$)

	Sh					*Nu*	R_t
	Le						
	0.1	0.3	1.0	3.0	10.0		
Trevisan and Bejan [12]	1.00	1.06	1.69	3.86	7.79	2.29	10^2
Present work	1.00	1.07	1.69	3.82	7.85	2.27	
Trevisan and Bejan [12]	1.04	1.34	3.37	8.61	17.17	6.11	10^3
Present work	1.04	1.34	3.32	8.40	16.98	6.06	
Trevisan and Bejan [12]	1.15	2.11	6.88	18.73	40.72	16.61	10^4
Present work	1.13	2.07	6.73	17.95	38.97	16.54	

5. Results and discussion

The foregoing analysis indicates that there are eight parameters that could be varied in this study. These are *Ra*, *N*, *Le*, *Da*, *Pr*, *AR*, *B* and *L*. Because of the abundance of parameters, a full-blown parametric investigation of the problem is unrealistic. The study is limited to a cavity with an aspect ratio of unity, i.e., a square enclosure ($AR = 1$). In the actual computations, *Ra* is fixed at 10^7, *Pr* is set equal to unity, *Le* is varied from 10^{-3} to 10^2. The buoyancy ratio *N* is in the range -15 to 14, covering the spectrum from solute-driven opposing flows ($N \ll -1$), to pure heat-driven flows ($N = 0$) and to solute-driven aiding flows ($N \gg 1$). The Brinkman extended Darcy model has been used through the study: in the first step, the Darcy number is fixed at 10^{-5}, and then the influence of the Brinkman term ($Da = 10^{-8}-10^{2}$) is analyzed. The length of heating and salting segment *B* is maintained at 1/4 and its position *L* would be varied from 0.875 to 0.125. The coordinates are chosen in the present work such that counterclockwise (or clockwise) movement will be associated with positive (or negative) streamfunctions. Due to the thermal and solutal boundary conditions considered here, the right side wall has a higher temperature and higher concentration than the left wall. As a result, the direction of the thermal flow is counterclockwise, whereas the direction of the solutal flow depends upon the sign of the concentration expansion coefficient β_s in Eq. (13). Thus the direction of the solutal flow is counterclockwise for $\beta_s(N) > 0$ and clockwise for $\beta_s(N) < 0$.

5.1. Combined effect of segment location and buoyancy ratio

The computed streamlines, isotherms, iso-concentrations, heatlines and masslines with $Le = 10$ and $Da = 10^{-5}$ are plotted in Figs. 2–4 for several combinations of segment location and buoyancy ratio. The flow directions in the graphs can be easily identified according to the distributions of temperature and concentration. The intervals of streamlines, isotherms, iso-concentration lines, heatlines and masslines are $\Delta\Phi = (\Phi_{max} - \Phi_{min})/16$, where Φ stands for Ψ, T, S, ξ or η.

First, the heat-driven flow limit ($N = 0$) depicted in Fig. 2 is discussed. For this situation, the ensuing flow is driven solely by the buoyancy effect associated with the temperature gradients, while the solutal contribution becomes negligible. As the heating segment is at the top of the wall (Fig. 2(a)), boundary layers start at $Y = 0.75$ and the center of rotation is located near the sink. The flow out the active element is subject to severe restriction imposed by the top wall. Because of this, most fluid flows at higher speed within the upper half of the enclosure, with weak flow in the lower one. The isotherms also show steeper gradients near the heating segment, while the concentration field that rides on the heat-transfer-driven flow as depicted in Fig. 2 depends to a significant degree on the Lewis number. For the fluid with relatively high Lewis number ($Le = 10 > 1$), the thermal boundary layer is expected to be much thicker than the hydrodynamic boundary layer, and the hydrodynamic boundary layer is either comparable to or thicker than the solute boundary layer. Additionally, at high Lewis number, the mass diffusivity is low enough relative to the thermal diffusivity so that the horizontal intrusion layers lining the top and bottom walls are considerably sharper than their thermal counterparts, the net result is that the concentration field in the core of the cavity is noticed to be almost uniform. Heatlines and masslines paralleling to the top wall indicate that the heat and solute transports from the source to the upper left wall directly. It is worth mentioning that Eqs. (18)–(19) suggest that the mass transport is more affected by the convection as $Le > 1$. As a result, the masslines of which the boundary layers and horizontal corridor are thinner than those of heatlines.

As the segment descends to the center, shown in Fig. 2(b), the core of the flow eddy is elongated horizontally. The isotherms are skewed towards the heating segment, and the temperature and concentration boundary layers start from the leading edge of the segment and the upper left-hand corner. The greater displacement of the isothermal bands from the segment indicates that the rate of heat transfer increases as the segment is lowered. This increase in heat transfer is associated with lessened drag across the top wall, and with more symmetrical and stronger circulation as illustrated by streamlines. At this time, the heatlines and masslines gradually exhibit a convex structure, i.e., the transportation path consisting of three sections: two thin boundary layers along the vertical walls and one horizontal corridor along the top adiabatic and impermeable wall. Within the boundary layer, fluid convection is weak and hence the diffusion prevails so that the flux lines are of pseudo-diffusion characteristics, as an illustration, the heatlines and masslines shown in Fig. 2(b) are perpendicular to the left wall, which is due to the fact that the potential functions in

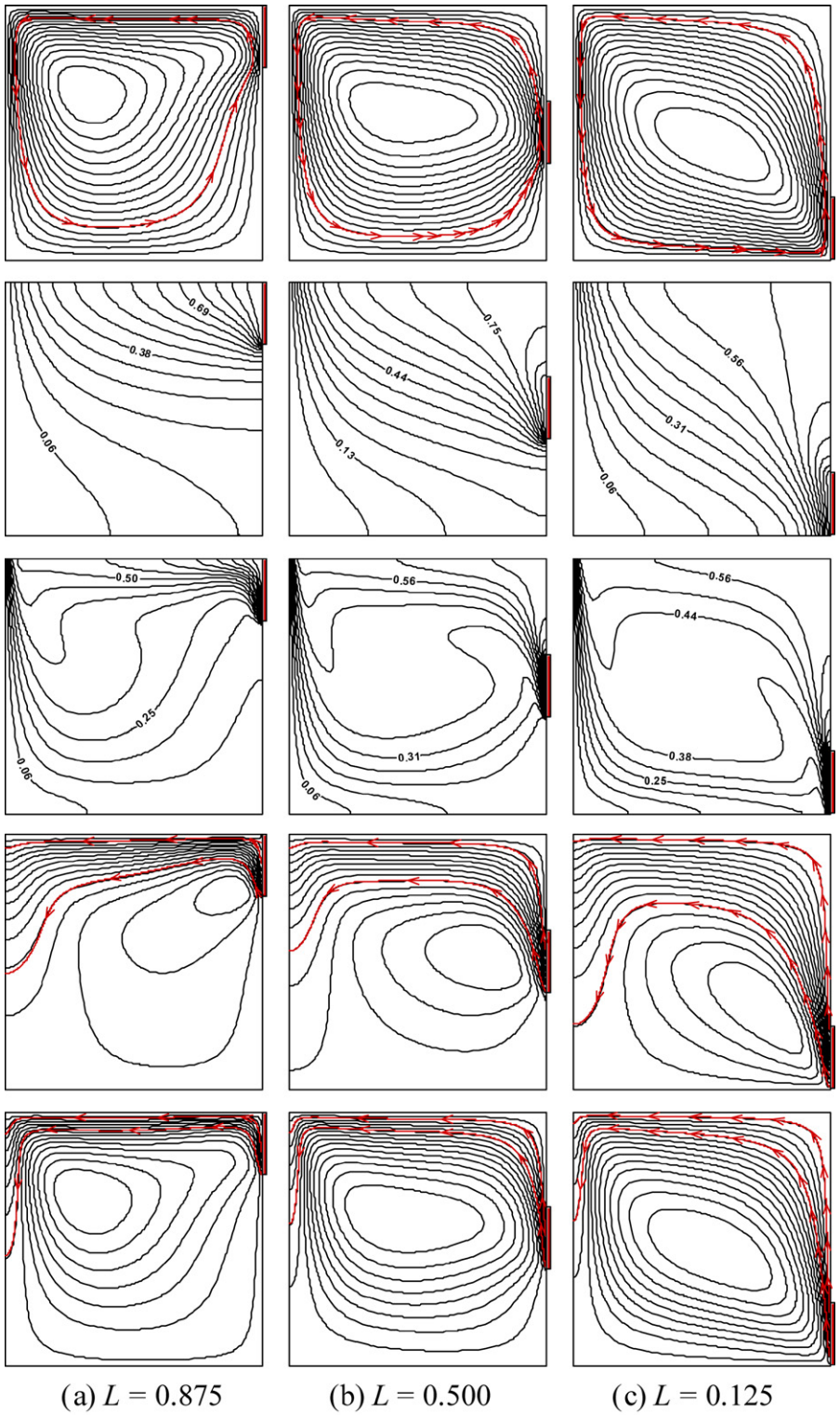

Fig. 2. Streamlines (top), isotherms (top-1), iso-concentrations (top-2), heatlines (top-3) and masslines (bottom) for the situation of heat-driven flow limit ($N = 0$) with $Le = 10$, $Da = 10^{-5}$. (a) $L = 0.875$, $\Psi_{\max} = 0.0007$, $\Psi_{\min} = 0.0000$, $\xi_{\max} = 0.277$, $\xi_{\min} = -1.067$, $\eta_{\max} = 4.460$, $\eta_{\min} = -5.509$; (b) $L = 0.500$, $\Psi_{\max} = 0.0011$, $\Psi_{\min} = 0.0000$, $\xi_{\max} = 0.629$, $\xi_{\min} = -1.951$, $\eta_{\max} = 9.461$, $\eta_{\min} = -8.145$; and (c) $L = 0.125$, $\Psi_{\max} = 0.0013$, $\Psi_{\min} = 0.0000$, $\xi_{\max} = 0.726$, $\xi_{\min} = -1.869$, $\eta_{\max} = 11.484$, $\eta_{\min} = -7.947$.

Eqs. (18)–(19) represent the relative strength between convection and diffusion.

The localized heating is positioned at the bottom of the enclosure covering the lower fourth of the wall shown in Fig. 2(c), a flow circulation oriented along the diagonal joining the left upper and right lower corners has been observed. The fluid mixture heated by the heating segment rises along the right wall and circulates to the left. It transfers its energy and constituent

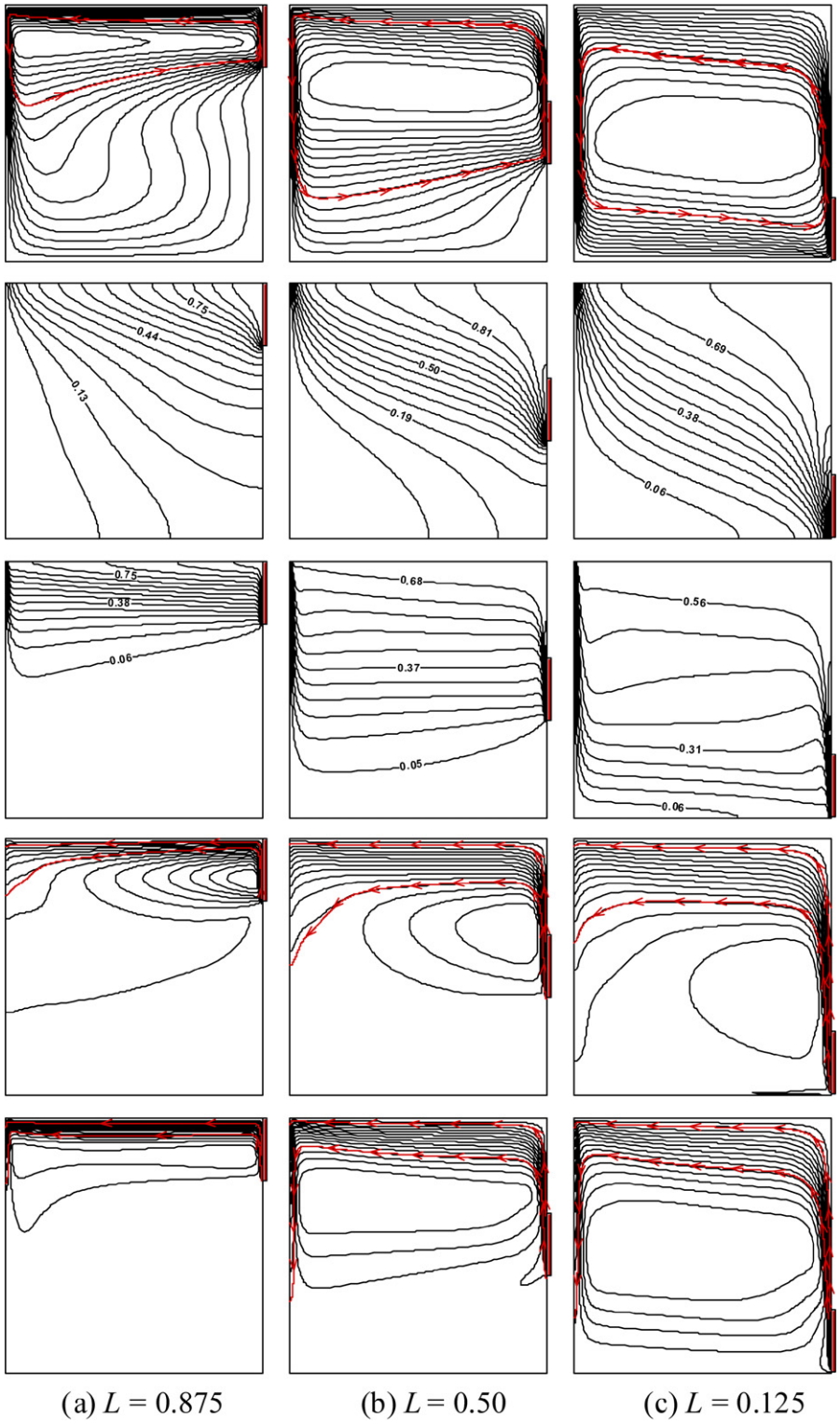

Fig. 3. Streamlines (top), isotherms (top-1), iso-concentrations (top-2), heatlines (top-3) and masslines (bottom) for aiding flows ($N = 8$) with $Le = 10$ and $Da = 10^{-5}$. (a) $L = 0.875$, $\Psi_{max} = 0.0007$, $\Psi_{min} = 0.0000$, $\xi_{max} = 0.838$, $\xi_{min} = -1.205$, $\eta_{max} = 2.092$, $\eta_{min} = -14.255$; (b) $L = 0.500$, $\Psi_{max} = 0.0014$, $\Psi_{min} = 0.0000$, $\xi_{max} = 0.875$, $\xi_{min} = -3.138$, $\eta_{max} = 6.571$, $\eta_{min} = -22.703$; and (c) $L = 0.125$, $\Psi_{max} = 0.0019$, $\Psi_{min} = 0.0000$, $\xi_{max} = 0.580$, $\xi_{min} = -4.121$, $\eta_{max} = 10.004$, $\eta_{min} = -23.871$.

to the sink by convection and returns to the segment, which has also been clearly illustrated by the heatlines and masslines in Fig. 2(c). The isotherms are becoming more vertical, while the iso-concentrations are becoming more uniform than stratified. The active area is the same in these cases, while the total dimensionless exit length downstream of the active zones (Ex) varies [25]. Ex has a value of 0, 0.375 and 0.75 in Fig. 2(a), Fig. 2(b) and Fig. 2(c) respectively. Circulation rates increase

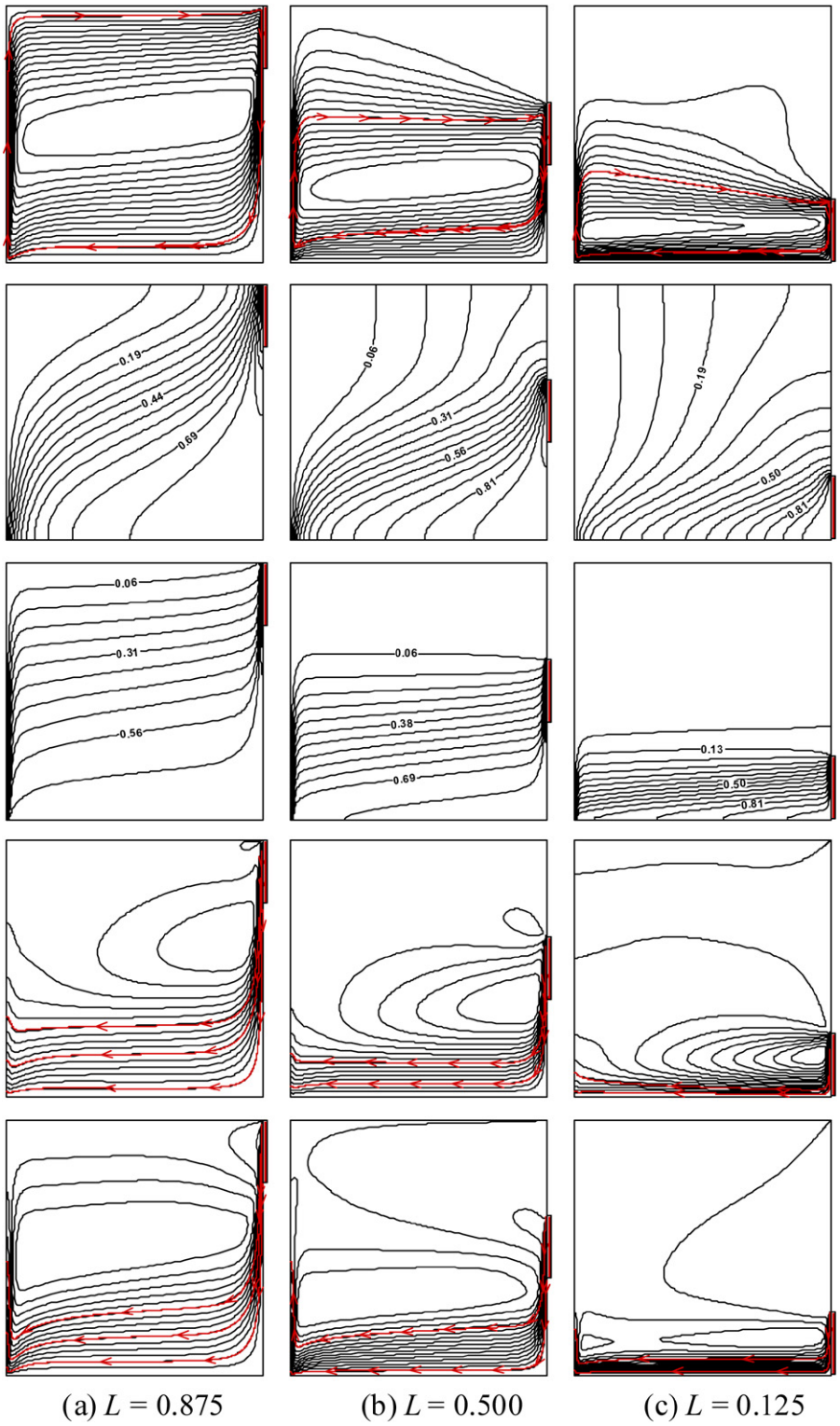

Fig. 4. Streamlines (top), isotherms (top-1), iso-concentrations (top-2), heatlines (top-3) and masslines (bottom) for opposing flows ($N = -10$) with $Le = 10$ and $Da = 10^{-5}$. (a) $L = 0.875$, $\Psi_{max} = 0.0000$, $\Psi_{min} = -0.0016$, $\xi_{max} = 0.000$, $\xi_{min} = -4.167$, $\eta_{max} = 0.013$, $\eta_{min} = -31.566$; (b) $L = 0.500$, $\Psi_{max} = 0.0000$, $\Psi_{min} = -0.0012$, $\xi_{max} = 0.002$, $\xi_{min} = -3.471$, $\eta_{max} = 0.021$, $\eta_{min} = -27.549$; and (c) $L = 0.125$, $\Psi_{max} = 0.0000$, $\Psi_{min} = -0.0006$, $\xi_{max} = 0.010$, $\xi_{min} = -1.795$, $\eta_{max} = 0.117$, $\eta_{min} = -15.081$.

with Ex, Fig. 2(c) gives the highest circulation rates.

Figs. 3(a)–(c) exemplify typical features of aiding double-diffusive flow ($N > 0$). When the buoyancy ratio is increased above zero the flow near the concentrated heating and salting segment is driven vertically upward, and meanwhile the low concentration at the left-hand wall causes the fluid near it to sink. As expected, both thermal and solutal buoyancy effects are augmenting each other and thus they simultaneously accel-

erate the flow counterclockwise. When the buoyancy ratio is increased to $N = 8$ (Fig. 3), the solutal buoyancy force greatly dominates over the thermal one, mass species dominated aiding flows arise. As the segment is at the top of the wall, a primary cell forms in the upper half enclosure shown in Fig. 3(a). The iso-concentrations show for this case, strong stratification in the upper region. Simultaneously, distributions of heatlines and masslines illuminate that the main heat and solute transfers are at the upper quarter of the cavity that accompanies formation of boundary layers on both sides. As the segment is at the middle of the wall (Fig. 3(b)), the concentration contours are vertically stratified within the core. Simultaneously, the resulting flow circulation is progressively restricted to thin boundary layers; a portion of the fluid in the center of the enclosure is now stagnant due to the stabilizing (blocking) effect of the vertical stratification of the density field in this area. As the segment shifts downward to the bottom of the enclosure (Fig. 3(c)), the primary cell is skewed toward the segment and grows in size. As a result, the fluid flows a longer path along the sink wall, more heat and solute is transferred through the wall, as demonstrated by more heatlines and masslines reach the left wall. Correspondingly, as the segment shifts downward from the top to the bottom, heat and mass transfer is greatly enhanced such that Nu increases from 1.205, 3.132 to 4.115, and Sh from 14.254, 22.657 to 23.835 respectively.

The typical feature of opposing double-diffusive flow ($N < 0$) is discussed herein. Fig. 4 provides exemplary results for a large buoyancy ratio ($N = -10$). The main contribution for buoyancy is due to the solutal one, and the fluid near the sink would be driven upward. The direction of the fluid circulation has been completely reversed and the flow pattern consists of a primary cell moving clockwise in the cavity. When the segment is at the top of the wall, a roll cell in the clockwise direction oriented along the diagonal joining the lower left and upper right corners is observed in Fig. 4(a). The isotherms are tilted clockwise by the primary cell, while the concentration contours are stratified within the core region spanned by the primary cell. It is observed from the heatlines and masslines that heat and solute flow from the segment to the lower-left sink through a thin region adjacent to the lower horizontal wall. This is a direct consequence of the natural convection resulting clockwise rotating flow. Differing from the convex transport structures presented in Figs. 2 and 3, the concave thermal and solutal transport structures arise, including two thin boundary layers along the vertical walls and one horizontal corridor along the bottom adiabatic and impermeable wall. As the segment shifts to the middle of the wall (Fig. 4(b)), a primary clockwise flow cell circulates in the lower region of the enclosure. The isotherms are becoming more vertical in the upper region, while the iso-concentrations are becoming more stratified than diagonal in the lower region. The solutal boundary layers along the lower left wall and the segment are thickening, which is indicative of decreasing solute transfer across the enclosure. Thus, when L decreases from 0.875 to 0.5, the total Sherwood and Nusselt numbers decrease about 20% and 10% respectively. When the segment is positioned at the bottom of the enclosure, as shown in Fig. 4(c), a primary roll cell arises in the lower region of the enclosure. The thermal buoyancy would start to exert some influence resulting in the flow pattern. More exactly, a small thermal cell can be presented in the upper right corner but its magnitude is so small that its presence is not observable in the streamline patterns of Fig. 4(c). On the other hand, for solute-dominated opposing flow, the fluid in the boundary layer adjacent to the segment should move downward from the bottom of the salting segment, while this stream faces the severe restriction of the bottom horizontal wall. Correspondingly, the total dimensionless exit length downstream of the active zones

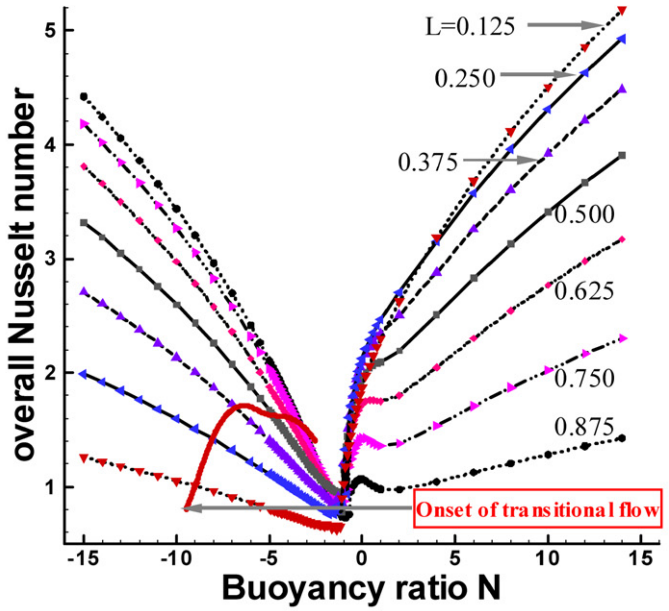

(a) *Nu*-*N*

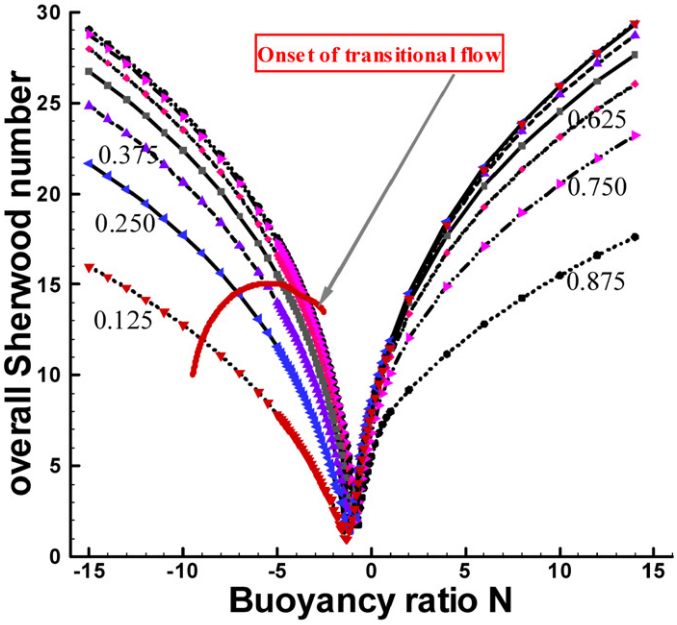

(b) *Sh*-*N*

Fig. 5. Overall Nusselt number Nu (a) and Sherwood number Sh (b) as functions of buoyancy ratio for the case $Le = 10$, $Da = 10^{-5}$ with the element location L as parameter.

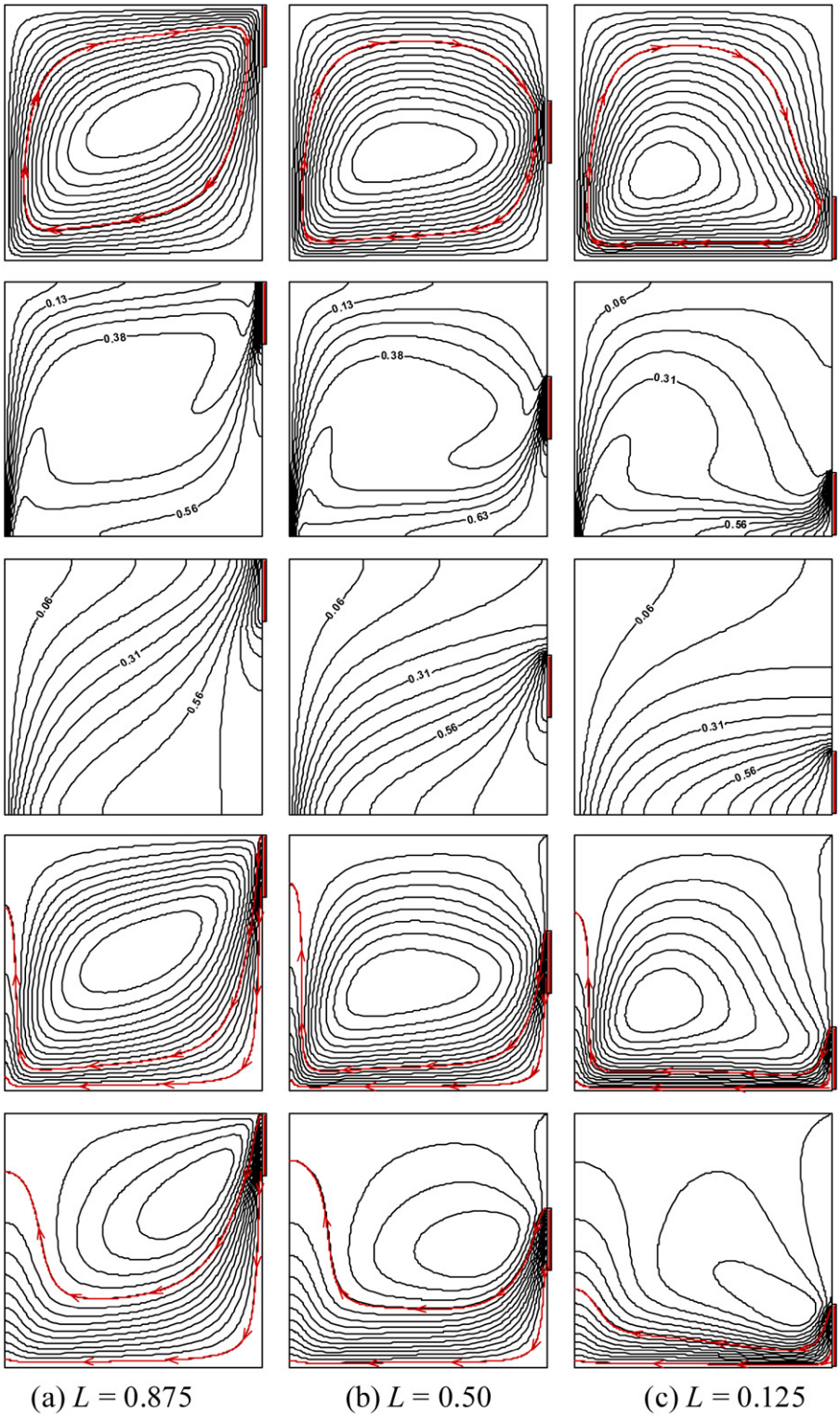

Fig. 6. Streamlines (top), isotherms (top-1), iso-concentrations (top-2), heatlines (top-3) and masslines (bottom) for opposing flows ($N = -10$) with $Da = 10^{-5}$, $Le = 0.1$. (a) $L = 0.875$, $\Psi_{max} = 0.0000$, $\Psi_{min} = -0.0126$, $\xi_{max} = 0.000$, $\xi_{min} = -18.980$, $\eta_{max} = 0.000$, $\eta_{min} = -2.522$; (b) $L = 0.50$, $\Psi_{max} = 0.0000$, $\Psi_{min} = -0.0109$, $\xi_{max} = 0.000$, $\xi_{min} = -17.302$, $\eta_{max} = 0.000$, $\eta_{min} = -2.489$; and (c) $L = 0.125$, $\Psi_{max} = 0.0000$, $\Psi_{min} = -0.0069$, $\xi_{max} = 0.009$, $\xi_{min} = -9.739$, $\eta_{max} = 0.000$, $\eta_{min} = -1.269$.

(Ex) would be markedly changed from the foregoing aiding cases, i.e., Ex has a value of 0.75 in Fig. 4(a), 0.375 in Fig. 4(b) and 0 in Fig. 4(c). As a result, Fig. 4(c) gives the lowest circulation rates (the maximum values of absolute streamfunctions). The effective heat and solute transport passages become thinner, as a result, when L decreases from 0.5 to 0.125, the total Nusselt and Sherwood numbers decrease from 2.598 to 1.053, from 22.371 to 12.761 respectively.

The combined effect of segment location and buoyancy ratio on the overall Nusselt and Sherwood numbers can be examined in Fig. 5. The graph clearly indicates that for aiding flows ($N > 0$), the transport rates increase with the magnitude of N, which is independent of segment location. As N is decreased below zero (opposing flow), initially the transport rates are observed to decrease with the magnitude of $|N|$ and become lower when compared with those with aiding buoyancies for the same numerical values of $|N|$. As N continues to decrease, the transport rates begin to increase because it is the magnitude of velocity and not the direction that augments the heat and mass transfer rates. As a result, *Nu* and *Sh* tend to be minimized in the transitional range to the point of flow reversal. The $N_{\min}$, corresponding to the minimum transport rates, is seen to depend strongly on the segment location. For $L \leqslant 0.5$, the overall Nusselt numbers are generally less in the opposing flow area ($N < 0$) than for the corresponding N in the aiding flow range due to the fact that the opposing flow has a lower flow rate adjacent to the sink than does the corresponding aiding flow case. However, for $L > 0.5$, the reversal is observed from the Fig. 5(a). However, the relative difference of Sherwood number for corresponding buoyancy ratios is small.

Transitional flow is in fact much more complex than the aiding flow illustrated in Figs. 2 and 3 and the solutal-dominated opposing flow in Fig. 4. For transitional flow, the thermal and solutal buoyancy forces dominate separate circulations within the enclosure. The onset of flow transition has been plotted in Figs. 5(a) and 5(b), representing the buoyancy ratio at which intrusion of the thermal dominated cell occurs. Upward movement of the heating and salting segment results in the decreasing of the buoyancy ratio at which this onset occurs. However, the point of flow reversal from transitional flow to thermal dominated flow first shifts to higher buoyancy ratios and then to lower buoyancy ratios for increasing L.

5.2. *Combined effect of segment location and Lewis number*

As N, L and Le equal -10, 0.875 and 0.1 respectively, the resulting flow presented in Fig. 6(a) is definitely solutal-dominated with a higher flow rate circulation than that in Fig. 4(a). The clockwise-rotating cell tilts and spans in the enclosure; Due to the blocking effect of the vertical stratification of the density field in this area, a constant temperature 'blob' develops with a large portion of the fluid is stagnant within the core of the enclosure; simultaneously, the heatlines illuminating the anti-natural thermal flow take the similar images as presented in Fig. 4(a) but with thinner horizontal corridor. With Lewis number less than unity, the mass transfer process is diffusion dominated. The solutal boundary layer is rather thick, and the iso-concentration lines are tilted with the segment location. The difference between the concentration and temperature fields is dictated by the Lewis number, in other words, the $T(\xi)$ and $S(\eta)$ fields are identical only in the special case $Le = 1$ [10, 29]. As Le is decreased to 0.1, the effect of solutal buoyancy force is strengthened for a constant buoyancy ratio. This is due to the increased diffusivity of the mass species, which results in the thickening of the solutal boundary layers. Consequently,

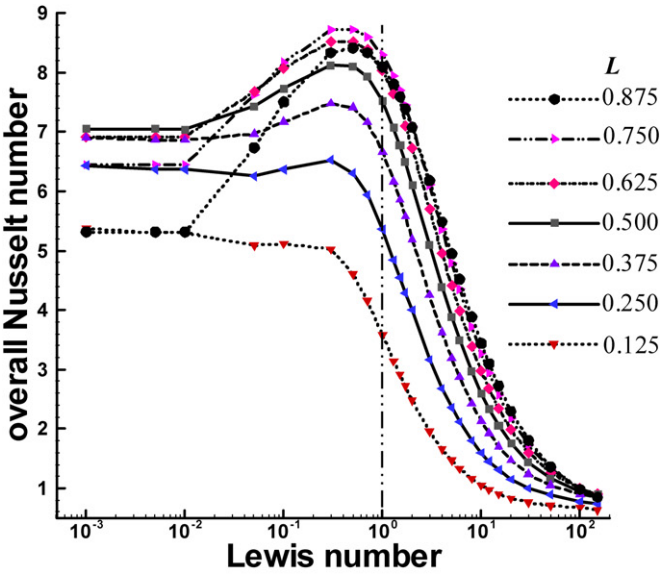

(a) *Nu-Le*

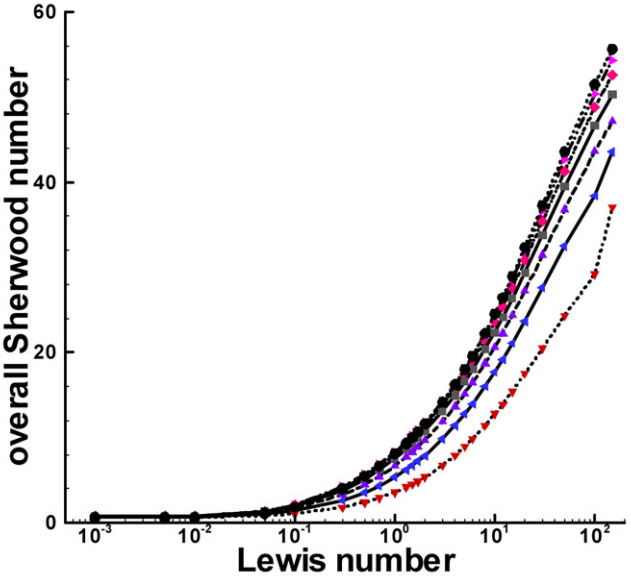

(b) *Sh-Le*

Fig. 7. Overall Nusselt number *Nu* (a) and Sherwood number *Sh* (b) as functions of Lewis number for the case $N = -10$, $Da = 10^{-5}$ with the element location L as parameter.

the effect of heat on the fluid density does not penetrate as far as the solutal fluid density effect. Similar observations can be made when comparing Fig. 6(b) with Fig. 4(b) ($L = 0.5$). As the segment shifts to the bottom, the transitional flow (at higher Lewis number) has completely reversed to the solutal dominated flow illustrated in Fig. 6(c). The solutal boundary layer becomes thicker and the mass species more diffused. The major mass transfer process is mass diffusion within the solutal boundary layer, while the thermal buoyancy exerts barely influence on the flow structures.

The Lewis number, which embraces the relative importance of thermal to solutal diffusion, has a direct bearing on the heat and mass transfer coefficients. The data in Fig. 7, obtained

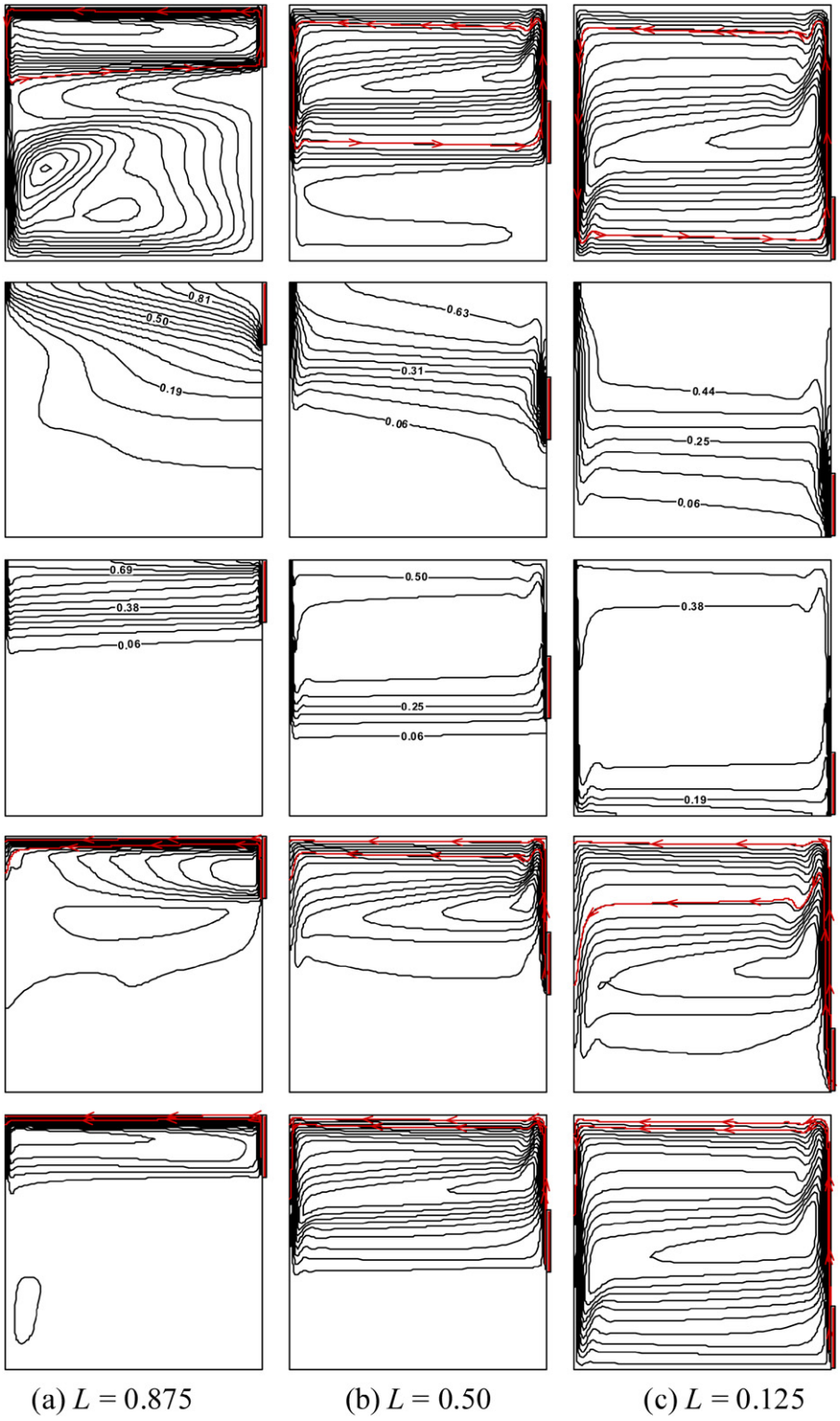

Fig. 8. Streamlines (top), isotherms (top-1), iso-concentrations (top-2), heatlines (top-3) and masslines (bottom) for aiding flows ($N = +8$) with $Da = 10^{-1}$, $Le = 10.0$. (a) $L = 0.875$, $\Psi_{max} = 0.0015$, $\Psi_{min} = 0.0000$, $\xi_{max} = 1.527$, $\xi_{min} = -2.692$, $\eta_{max} = 10.638$, $\eta_{min} = -23.221$; (b) $L = 0.500$, $\Psi_{max} = 0.0062$, $\Psi_{min} = -0.0001$, $\xi_{max} = 4.037$, $\xi_{min} = -8.422$, $\eta_{max} = 58.771$, $\eta_{min} = -31.521$; and (c) $L = 0.125$, $\Psi_{max} = 0.0093$, $\Psi_{min} = 0.0000$, $\xi_{max} = 4.003$, $\xi_{min} = -10.295$, $\eta_{max} = 77.056$, $\eta_{min} = -33.719$.

for $N = -10$ and $Da = 10^{-5}$, span the Lewis number range 10^{-3}–10^{2}. The concentration boundary layers become increasingly thinner as Le increases. As a result, for a given N and Da, the Sherwood number consistently increases as the Lewis number increases. However, overall Nusselt number decrease with increasing Le is due to the fact that the thermal boundary layer thickness is an increasing function of $Le^{1/2}$ [3]. The role-played by the segment location on the overall Nusselt and Sherwood

numbers is also illustrated in Fig. 7. As L is no more than 0.5, this issue is of singular importance on both transfer coefficients in the considered Lewis number range, the curves of $L \leqslant 0.500$ generally tend to converge a critical value as Le increases far greater than unity. However, for $Le < 1.0$, the flow is mainly driven by the action of a solutal buoyant force. The effect of location L on the overall Nusselt number is similar to that of lower Rayleigh number (pure diffusion regime). Similar observations can be found for overall Sherwood number due to the dominated solutal diffusion.

5.3. Combined effect of segment location and Darcy number

In this section, the influence of the porous-medium coarseness ($10^{-8} \leqslant Da \leqslant 10^{2}$) on the double diffusion is investigated. The buoyancy ratio and Lewis number is maintained at 8 and 10 respectively. As Darcy number increases from 10^{-5} (Fig. 3) to 10^{-1} (Fig. 8) with L equaling 0.875, the effect of the viscous forces accounted for in the Brinkman term on the flow velocity becomes significant. For this moderately high buoyancy ratio ($N = 8$), a multicellular flow structure is observed in the lower half of the cavity. The streamlines show that the dynamic boundary layers are thinner for the higher value of Da, and consequently the concentration gradients at the walls are larger when the Brinkman term becomes significant. The concentration field presents the classical stratified structure of the natural convective flows in enclosures; the isotherms also show more stratified than inclined. As the segment shifts down, the aforementioned trends are aggravated.

The effect of varying the Darcy number on the heat and mass transfer, Nu and Sh are illustrated in Fig. 9 for various segment locations. As the permeability of the porous medium Da is increased, the boundary frictional resistance becomes gradually less important and the fluid circulation within the enclosure is progressively enhanced. Indeed, increasing the Brinkman term implies that the balance between the Darcy term and the buoyancy force in the boundary layer is progressively replaced by the balance between a viscous force and the buoyancy term. The viscous force enhances the velocity at high Darcy numbers. The results indicate that when Da is large enough, Nu and Sh tend asymptotically toward constant values that depend on the segment location. The limit $Da \to 0$ corresponds to a pure Darcy medium situation which has been studied recently by Zhao et al. [26]. As a result, Nu and Sh are observed to decrease considerably with decreasing Da toward the pure conduction limit. This is expected since, in the limit of Da approaching 0, the Brinkman model reduces to Darcy Law. As the Darcy number is decreased, the boundary frictional resistance becomes progressively significant and adds to the bulk frictional drag induced by the solid matrix to slow the convection motion. Indeed, as comparing Fig. 8 and Fig. 3, it is found that the strength of the overall convective flow becomes weaker as the value of Da is made smaller.

6. Conclusions

The problem of double-diffusive convective flow of a binary mixture inside a vertical enclosure subject to localized heating and salting from one side is numerically studied. Finite volume method is employed on non-uniform grids for the solution of the present problem. The obtained heatlines and masslines, for the double diffusive natural convection in porous medium are shown to be a very effective way to visualize the paths followed by heat and solute through this porous enclosure.

A complete range of buoyancy ratios, covering solute-dominated opposing flow, transitional flow, thermal-dominated flow and solute-dominated aiding flow, is examined for several segment locations. Upward movement of the segment results in the decreasing of the buoyancy ratio at which the onset of transitional flow occurs. Overall heat and mass transfer rates tend

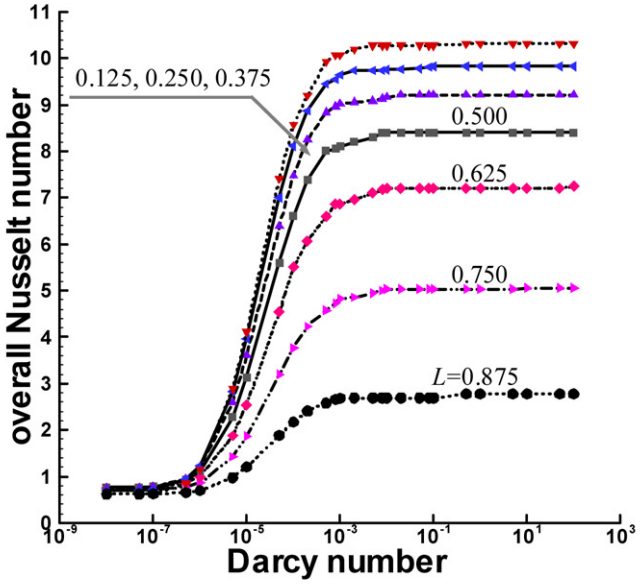

(a) *Nu-Da*

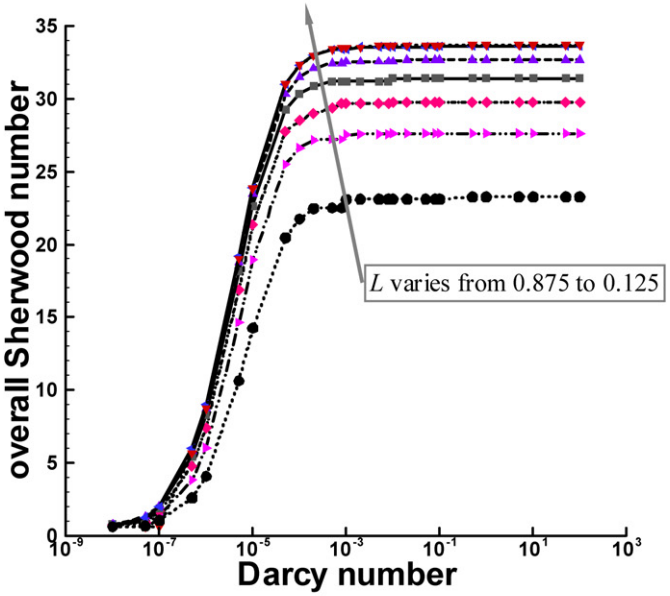

(b) *Sh-Da*

Fig. 9. Overall Nusselt number Nu (a) and Sherwood number Sh (b) as functions of Darcy number for the case $N = +8$, $Le = 10$ with the element location L as parameter.

to be minimized in the transitional range to the point of flow reversal for any segment location.

Effects of Lewis number and Darcy number on the double diffusive convection have also been examined for several segment locations. Reversion of transitional flow to the solutal-dominated flow tends to occur at higher Lewis number for lower-level segment locations. As the permeability the porous medium is decreased, the temperature and concentration contours become more parallel to the vertical walls, indicating the approach to quasi-conduction regime. The main contributions of decreasing the Darcy number are predicted to be a flow retardation effect and a suppression of the overall heat and mass transfer in the enclosure.

Acknowledgements

This research work was financially supported by a grant from the Natural Science Foundation of China (NSFC No. 50578059). The authors are also grateful to the anonymous referees who provided detailed and constructive comments.

References

[1] D.B. Ingham, I. Pop (Eds.), Transport Phenomena in Porous Media, Elsevier, Oxford, 2005.
[2] O.V. Trevisan, A. Bejan, Natural convection with combined heat and mass transfer buoyancy effects in a porous medium, Int. J. Heat Mass Transfer 28 (1985) 1597–1611.
[3] B. Goyeau, J.P. Songbe, D. Gobin, Numerical study of double-diffusive natural convection in porous cavity using the Darcy–Brinkman formulation, Int. J. Heat Mass Transfer 39 (1996) 1363–1378.
[4] M. Mamou, P. Vasseur, E. Bilgen, A Galerkin finite-element study of the onset of double-diffusive convection in an inclined porous enclosure, Int. J. Heat Mass Transfer 41 (1998) 1513–1529.
[5] H. Beji, R. Bennacer, R. Duval, P. Vasseur, Double-diffusive natural convection in a vertical porous annulus, Numer. Heat Transfer, Part A 36 (1999) 153–170.
[6] R. Bennacer, H. Beji, R. Duval, P. Vasseur, The Brinkman model for thermosolutal convection in a vertical annular porous layer, Int. Comm. Heat Mass Transfer 27 (2000) 69–80.
[7] R. Bennacer, A. Tobbal, H. Beji, P. Vasseur, Double diffusive convection in a vertical enclosure filled with anisotropic porous media, Int. J. Thermal Sci. 40 (2001) 30–41.
[8] A.J. Chamkha, H. Al-Naser, Double-diffusive convection in an inclined porous enclosure with opposing temperature and concentration gradients, Int. J. Thermal Sci. 40 (2001) 227–244.
[9] A.J. Chamkha, Double-diffusive convection in a porous enclosure with cooperating temperature and concentration gradients and heat generation or absorption effects, Numer. Heat Transfer, Part A 41 (2002) 65–87.
[10] V.A.F. Costa, Double-diffusive natural convection in parallelogrammic enclosures filled with fluid-saturated porous media, Int. J. Heat Mass Transfer 47 (2004) 2699–2714.
[11] A.A. Mohamad, R. Bennacer, J. Azaiez, Double diffusion natural convection in a rectangular enclosure filled with binary fluid saturated porous media: the effect of lateral aspect ratio, Phys. Fluids 16 (1) (2004) 184–199.
[12] O.V. Trevisan, A. Bejan, Mass and heat transfer by natural convection in a vertical slot filled with porous medium, Int. J. Heat Mass Transfer 29 (1986) 403–415.
[13] F. Alavyoon, On natural convection in vertical porous enclosures due to prescribed fluxes of heat and mass at the vertical boundaries, Int. J. Heat Mass Transfer 36 (1993) 2479–2498.
[14] F. Alavyoon, Y. Masuda, S. Kimura, On natural convection in vertical porous enclosures due to opposing fluxes of heat and mass prescribed at the vertical walls, Int. J. Heat Mass Transfer 37 (1994) 195–206.
[15] M. Mamou, P. Vasseur, E. Bilgen, Multiple solutions for double-diffusive convection in a vertical porous enclosure, Int. J. Heat Mass Transfer 38 (1995) 1787–1798.
[16] M. Mamou, P. Vasseur, E. Bilgen, Double-diffusive convection instability in a vertical porous enclosure, J. Fluid Mech. 368 (1998) 263–289.
[17] A. Amahmid, M. Hasnaoui, M. Mamou, P. Vasseur, Boundary layer flows in a vertical porous enclosure induced by opposing buoyancy forces, Int. J. Heat Mass Transfer 42 (1999) 3599–3608.
[18] M. Marcoux, M.-C. Charrier-Mojtabi, M. Azaiez, Double-diffusive convection in an annular vertical porous layer, Int. J. Heat Mass Transfer 42 (1999) 2313–2325.
[19] M. Mamou, Stability analysis of thermosolutal convection in a vertical packed porous enclosure, Phys. Fluids 14 (12) (2002) 4302–4314.
[20] B.V.R. Kumar, P. Singh, V.J. Bansod, Effect of thermal stratification on double-diffusive natural convection in a vertical porous enclosure, Numer. Heat Transfer, Part A 41 (2002) 421–447.
[21] B.V.R. Kumar, Shalini, Double-diffusive natural convection in a doubly stratified wavy porous enclosure, Appl. Math. Comput. 171 (2005) 180–202.
[22] F.Y. Zhao, D. Liu, G.F. Tang, Resonant response of fluid flow subjected to discrete heating elements, Energy Conversion Management (2007), in press, doi:10.1016/j.enconman.2007.04.008.
[23] N.H. Saeid, Natural convection from two thermal sources in a vertical porous layer, J. Heat Transfer 128 (2006) 104–109.
[24] M. Bourich, M. Hasnaoui, A. Amahmid, Double-diffusive natural convection in a porous enclosure partially heated from below and differentially salted, Int. J. Heat Fluid Flow 25 (2004) 1034–1046.
[25] W. Chen, F.Y. Zhao, G.F. Tang, D. Liu, Transportation of indoor double diffusive mixed convection coupled with diffusion in solid walls, Journal of HV&AC 36 (8) (2006) 12–18.
[26] F.Y. Zhao, D. Liu, G.F. Tang, Free convection from one thermal and solute source in a confined porous medium, Transport in Porous Media (2007), doi:10.1007/s11242-007-9106-7.
[27] V.A.F. Costa, Unified streamline, heatline and massline methods for the visualization of two-dimensional heat and mass transfer in anisotropic media, Int. J. Heat Mass Transfer 46 (2003) 1309–1320.
[28] F.Y. Zhao, D. Liu, G.F. Tang, Conjugate heat transfer in square enclosures, Heat Mass Transfer 43 (2007) 907–922.
[29] F.Y. Zhao, D. Liu, G.F. Tang, Application issues of the streamline, heatline and massline for conjugate heat and mass transfer, Int. J. Heat Mass Transfer 50 (2007) 320–334.
[30] V.A.F. Costa, Bejan's heatlines and masslines for convection visualization and analysis, Appl. Mech. Rev. 59 (2006) 126–145.
[31] F.Y. Zhao, G.F. Tang, D. Liu, Conjugate natural convection in enclosures with external and internal heat sources, Int. J. Eng. Sci. 44 (2006) 148–165.
[32] D. Liu, F.Y. Zhao, G.F. Tang, Conjugate heat transfer in an enclosure with a centered conducting body imposed sinusoidal temperature profiles on one side, Numer. Heat Transfer, Part A (2007), in press.
[33] S.V. Patankar, Numerical Heat Transfer and Fluid Flow, Hemisphere/McGraw-Hill, Washington, DC, 1980.
[34] T. Hayase, J.A.C. Humphrey, R. Greif, A consistently formulated QUICK scheme for fast and stable convergence using finite-volume iterative calculation procedure, J. Comput. Phys. 98 (1992) 108–118.
[35] D. Liu, F.Y. Zhao, G.F. Tang, Thermosolutal convection in a saturated porous enclosure with concentrated energy and solute sources, Energy Conversion Management (2007), in press.